

Alma Mater Studiorum Università di Bologna
Archivio istituzionale della ricerca

“Brittle structural facies” analysis: A diagnostic method to unravel and date multiple slip events of long-lived faults

This is the final peer-reviewed author’s accepted manuscript (postprint) of the following publication:

Published Version:

Tartaglia, G., Viola, G., van der Lelij, R., Scheiber, T., Ceccato, A., Schonenberger, J. (2020). “Brittle structural facies” analysis: A diagnostic method to unravel and date multiple slip events of long-lived faults. EARTH AND PLANETARY SCIENCE LETTERS, 545, 1-14 [10.1016/j.epsl.2020.116420].

Availability:

This version is available at: <https://hdl.handle.net/11585/765469> since: 2020-07-09

Published:

DOI: <http://doi.org/10.1016/j.epsl.2020.116420>

Terms of use:

Some rights reserved. The terms and conditions for the reuse of this version of the manuscript are specified in the publishing policy. For all terms of use and more information see the publisher's website.

This item was downloaded from IRIS Università di Bologna (<https://cris.unibo.it/>).
When citing, please refer to the published version.

(Article begins on next page)

**“Brittle structural facies” analysis: A diagnostic method to unravel and date
multiple slip events of long-lived faults**

Giulia Tartaglia^{a*}, Giulio Viola^{a*}, Roelant van der Lelij^b, Thomas Scheiber^c, Alberto
Ceccato^a, Jasmin Schönenberger^b

^a Dipartimento di Scienze Biologiche, Geologiche ed Ambientali – BiGeA, Università degli
studi di Bologna, Via Zamboni 67, 40126 Bologna, Italy

^b Geological Survey of Norway, 7491 Trondheim, Norway

^c Western Norway University of Applied Sciences, Department of Environmental Sciences,
Sogndal, Norway

*Corresponding authors:

Giulia Tartaglia, giulia.tartaglia4@unibo.it Via Zamboni 67, 40126, Bologna, Italy

Giulio Viola, giulio.viola3@unibo.it Via Zamboni 67, 40126, Bologna, Italy

Giulia Tartaglia: giulia.tartaglia4@unibo.it

Giulio Viola: giulio.viola3@unibo.it

Roelant van der Lelij: roelant.vanderlelij@ngu.no

Thomas Scheiber: thomas.scheiber@hvl.no

Alberto Ceccato: alberto.ceccato@unibo.it

Jasmin Schönenberger: jasmin.schonenberger@ngu.no

Abstract

Large faults typically experience complex, long-lasting histories, commonly recording
evidence of multiple reactivation events. Therefore, faults contain multiscalar structural
domains characterised by varying microstructures, mineralogical compositions and
kinematics. These domains result from differential strain partitioning during the recorded

25 faulting stages, and, as a result, can preserve the isotopic and kinematic signature of the
26 different slip periods. Their detailed structural analysis integrated with K-Ar dating of the
27 fault rock assemblage can help to identify these commonly tightly juxtaposed, although not
28 coeval, domains, which we refer herein to as “Brittle Structural Facies” (BSF). BSF
29 analysis is pivotal (i) to understand the structural heterogeneity of fault zones, (ii) the
30 diachronic formation of geometrically and kinematically complex fault cores and (iii) to
31 reconstruct faults’ evolution in time and through space. Following this approach, this study
32 relies on meso- and microstructural analysis, chemical characterisation and K-Ar dating to
33 unravel the evolution of the Lærdal-Gjende Fault (LGF, southwestern Norway). The LGF is
34 a multiply reactivated top-to-the-NW extensional fault with a 1 m thick poorly consolidated
35 core. We recognised, sampled and characterised five BSF: I) Indurated dark reddish
36 gouge, (II) Poorly consolidated cataclasite, (III) Weakly foliated greenish gouge, (IV) Clay-
37 rich gouge and (V) A few mm-thick clay smear decorating the principal slip surface.
38 Samples were separated into five grain size fractions (from <0.1 to $6-10\ \mu\text{m}$) and analysed
39 by X-Ray Diffraction, Transmission Electron Microscopy and K-Ar geochronology. A c. 180
40 Ma age cluster defined by 10 ages of the coarsest grain size fractions ($2-10\ \mu\text{m}$) likely
41 documents fault nucleation during Jurassic rifting in the North Sea. The ages of the finest
42 fractions, enriched in synkinematic K-bearing minerals (illite, smectite and K-feldspar),
43 constrain four periods of faulting at c. 121 ± 3 , 87 ± 2 , 78 ± 2 and 57 ± 1 Ma. Ages indicate that
44 the LGF accommodated strain due to hyperextension of the Mid-Norwegian margin down
45 to the Late Cretaceous and finally slipped again during the Paleogene. The alternating
46 widening and narrowing of the active fault zone in response to varying deformation
47 mechanisms, including coseismic rupturing, formed the present complex fault architecture.
48 This study highlights the importance of BSF characterisation as part of a multidisciplinary
49 workflow to derive structural and temporal datasets of complex fault zones. BSF analysis,

50 moreover, is demonstrated to be key for investigating the diachronic evolution of fault
51 cores and to resolve multiple slip events of long-lived faults.

52 **Keywords:** Brittle deformation, Brittle Structural Facies (BSF), K-Ar fault rock dating,
53 Strain localization.

54 **1. Introduction and aims of the study**

55 Fault zones are expression of brittle deformation in the Earth upper crust, where slip
56 localises in response to stresses that exceed the rock strength. Their nucleation and
57 progressive growth lead to the formation of fault cores and surrounding damage zones
58 (Chester and Logan, 1986; Caine et al., 1996). Different fault-related rocks, such as
59 cataclasite, breccia, gouge and pseudotachylyte, may commonly coexist within the same
60 fault zone. Their juxtaposition reflects the temporal and spatial evolution of the fault
61 system, including its deformation mechanisms and physical conditions at the time of initial
62 faulting, as well as of possible reactivations.

63 Many brittle faults can be interpreted as the summation of multiple deformation events
64 through time. During each faulting episode, slip and strain localisation lead to progressive
65 comminution of the host rock and synkinematic crystallisation of new minerals, such as
66 clays and phyllosilicates. Importantly, *in situ* synkinematic neoblastesis offers the
67 possibility to radiometrically date a given faulting event as well as later multiple
68 reactivations (e.g. van der Pluijm et al., 2001; Pleuger et al., 2012; Bense et al., 2013;
69 Davids et al., 2013; Yamasaki et al., 2013; Torgersen et al., 2015a; Ksienzyk et al., 2016;
70 Viola et al., 2016, 2018; Aldega et al., 2019; Scheiber et al., 2019).

71 Unravelling the relationships between mineral assemblages, age and kinematic framework
72 of all recorded slip events within a fault remains an arduous task (Clauer, 2013; Torgersen
73 et al., 2015a; Viola et al., 2016; Scheiber et al., 2019). The intrinsic complexity of faults

74 and the spatial arrangement of fault rocks reflect the interplay of fluid-rock interaction and
75 the ease of reactivation of brittle structures. The reactivation of suitably oriented faults
76 (Holdsworth, 2004) may lead to the partial or total obliteration of any inherited evidence of
77 earlier deformation events (Viola et al., 2013). Due to these complexities, conceptual
78 evolutionary models of fault zones do not always consider the absolute temporal
79 dimension of faulting, and thus become rather static snapshots of what is instead a
80 dynamic evolution. The lack of details on the temporal dimension of faulting may lead to
81 oversimplifications of the evolution of faults, which, in turn, can lead to a misinterpretation
82 of their possible seismic behaviour and overall tectonic role in the regional framework.

83 The necessity of a time-constrained reconstruction of faults' evolution has therefore led
84 structural geologists to study in detail their internal architecture (e.g. Caine et al., 1996;
85 Aydin, 2000), which often contains juxtaposed domains characterised by different fault
86 rocks, mineralogical composition, texture and kinematics. Multiple faulting events cause
87 deformation to preferentially localise into weaker volumes and along slip surfaces,
88 whereas lithons representing remnants of former slip events can be preserved. These
89 domains generally exhibit sharp boundaries and complex crosscutting relationships whose
90 unravelling is crucial to establish a relative temporal sequence of (de)formation. We apply
91 inhere the term "Brittle Structural Facies" (BSF) to refer to such domains (cf. Braathen et
92 al., 2009). In this paper, BSF specifically refers to a deformed volume of rock
93 characterised by a given fault rock type, texture, colour, composition, and age of formation.
94 The identification, structural analysis, mineralogical characterisation and radiometric dating
95 of BSF are key to (i) understand the structural heterogeneity of fault zones, (ii) decipher
96 the diachronic formation of geometrically and kinematically complex fault cores and (iii)
97 resolve the evolution of multiply reactivated faults.

98 To document our approach and the usefulness of the BSF concept, we present a
99 structural-geochronological workflow that serves as an example of general validity when
100 aiming to unravel the evolution of long-lived faults. We studied the Lærdal-Gjende Fault
101 (LGF), a multiply reactivated extensional fault in southwestern Norway (Andersen et al.,
102 1999; Fossen and Hurich, 2005; Fossen et al., 2016). The detailed structural analysis of
103 the fault core allowed us to identify five distinct BSF, and to sort out their mutual geometric
104 and relative temporal relationships. Samples from each brittle fault facies were
105 characterised by optical and Scanning Electron Microscopy (SEM). K-bearing phases from
106 fault rock samples were identified, quantified and characterised by X-Ray Diffraction (XRD)
107 and Transmission Electron Microscopy (TEM) and, finally, dated by the K-Ar technique.
108 This comprehensive structural, compositional and geochronological dataset has been
109 used to propose an evolutionary scheme of LGF that accounts for all dated faulting stages.

110 **2. Geological framework**

111 The study area is in southwestern Norway, near the town of Lærdal (Fig. 1a). There, the
112 Baltic autochthonous basement is overlain by Caledonian Allochthons (Corfu et al., 2014)
113 thrust south-eastward during the Late Silurian-Early Devonian Caledonian collision
114 between Baltica and Laurentia (Fossen and Dunlap, 1998). The autochthonous basement
115 is mainly composed of Mesoproterozoic migmatites that were only marginally affected by
116 Caledonian deformation (Fossen and Hurich, 2005). The Allochthons are tectonic nappes
117 derived from the cover sequences of the Baltic Shield, the ancient Iapetus Ocean and
118 Laurentian basement cover units. The allochthonous unit at the Lærdal site is formed by
119 the Laurentia-derived Jotun Nappe Complex. It is composed of a series of thrust sheets of
120 variously deformed plutonic rocks metamorphosed under amphibolite facies conditions
121 during the Proterozoic Sveconorwegian orogeny (Milnes and Corfu, 2011; Corfu et al.,

122 2014). The Jotun Nappe Complex comprises monzonitic and mangeritic orthogneiss,
123 metagabbroic slivers and anorthositic suites (Milnes and Corfu, 2011).

124 Caledonian collisional tectonics led to an over-thickened orogenic pile that collapsed
125 during the Early Devonian (408-402 Ma; Fossen and Dunlap, 1998) through the nucleation
126 and reactivation of orogen-scale extensional detachments. NW-SE extension caused the
127 exhumation of the orogenic roots to shallow crustal levels. The progressive
128 accommodation of deformation in the brittle regime led to the nucleation of major faults
129 and brittle fault zones, which overprinted earlier ductile detachments (Fossen et al., 2016).
130 One of these Devonian extensional detachments is the Hardangerfjord Shear Zone (HSZ),
131 which is exposed in the study area (Fig. 1a, Fossen et al., 2016). The HSZ is a gently
132 oblique top-to-the-NW shear zone (Fossen and Hurich, 2005), which is composed at the
133 Lærdal site of tens of meter thick mylonites separating the autochthonous basement from
134 the overlying Jotun Nappe Complex (Fig. 1a). The Lærdal-Gjende Fault strikes NE-SW,
135 and at its most representative outcrop in Lærdal it partially reworked and overprinted the
136 mylonitic fabric of the HSZ (Fig. 1a, Fossen and Hurich, 2005).

137 Thermochronological studies indicate that two main episodes of enhanced, rapid
138 exhumation affected southwestern Norway in the Permo-Triassic and in the late
139 Cretaceous-Cenozoic (Johannessen et al., 2013; Walsh et al., 2013; Ksienzyk et al.,
140 2014, 2016). During the Cretaceous, exhumation generated a high relief that was later
141 periodically rejuvenated by brittle faulting (Johannessen et al., 2013).

142 Two studies have focused on the age of brittle deformation along the LGF. Andersen et al.
143 (1999) studied the greenish epidote-rich cataclasite in the damage zone and constrained
144 Early Triassic up to Early Cretaceous slip by paleomagnetic techniques. Fossen et al.
145 (2016) used K-Ar radiometric dating on synkinematic illite from two fault core gouge
146 samples reporting dates between 200 and 64 Ma. In general, previous authors agree that

147 the LGF nucleated and developed as the shallow crustal brittle expression of the ductile
148 HSZ during the Devonian (although direct geochronological constraints on this episode are
149 not reported), and continued its activity until the Cretaceous, to around 120 Ma. Hence,
150 according to published data, the LGF was active during the post-collisional collapse of the
151 Caledonides and during the Mesozoic North Sea rifting evolution (Andersen et al., 1999;
152 Fossen and Hurich, 2005; Fossen et al., 2016). These studies, however, did not aim at
153 linking the different fault structural facies to their ages, and a time-constrained evolutionary
154 model of the LGF has not yet been proposed.

155 **3. Methods**

156 Our study is based on a combined structural-geochronological approach (Viola et al.,
157 2016) wherein a detailed structural analysis of the fault was done by identifying, describing
158 and characterising different BSF. Characterisation of the BSF and structural analysis were
159 performed along the entire LGF outcrop exposed in Lærdal (Fig. 1). Sample collection was
160 from the central part of the LGF outcrop, in a well exposed c. 1 m² portion of the fault core
161 (Fig. 1c). C. 400 g of variably consolidated fault rock material was collected for each BSF
162 (Fig. 1d). Special care was taken to avoid mixing between different BSF. Oriented samples
163 of consolidated fault rock and wall rock were collected for microstructural analysis. Thin
164 sections oriented parallel to the transport direction and perpendicular to the planar fabric
165 were prepared from the poorly consolidated samples of cataclasite and indurated gouge.
166 They were studied by optical and scanning electron microscopy equipped with an energy
167 dispersive X-ray analyser (SEM-EDS) at the University of Padua (Italy) to investigate
168 microstructure and mineralogical composition of the fault rocks.

169 Characterisation of the samples for K-Ar radiometric dating was performed at the
170 laboratories of the Geological Survey of Norway (Trondheim, Norway) following the
171 routines described by Viola et al. (2018). Samples from each BSF were disintegrated by

172 repeated freezing and thawing cycles. This method avoids artificial grain size reduction of
173 coarse-grained minerals and their contamination in the finer fractions. Samples were
174 separated in five grain size fractions (<0.1 , $0.1-0.4$, $0.4-2$, $2-6$ and $6-10$ μm). Grain size
175 fractions of <2 , $2-6$ and $6-10$ μm were separated in distilled water using Stokes' law,
176 whereas the finer fractions (<0.1 , $0.1-0.4$ and $0.4-2$ μm) were obtained by high speed
177 centrifugation of the <2 μm fraction.

178 The mineralogical composition of each grain size fraction for each sample was obtained by
179 XRD analysis (with a Bruker D8 Advance diffractometer). Mineral quantification was
180 carried out on randomly prepared specimens using Rietveld modelling with the TOPAS 5
181 software. Refined parameters include crystallite size, unit cell dimensions, sample
182 displacement, preferred orientation and background coefficients. The lower limit of
183 quantification and accuracy are mineral-dependent but are generally 1 wt% and 2-3 wt%,
184 respectively. The finest <0.1 μm grain size fractions could not be analysed by XRD due to
185 too low sample mass being recovered from these fractions. Detection and imaging of K-
186 bearing phases therein were thus carried out with a TEM (JEOL JEM-2100) equipped with
187 an energy dispersive X-ray analyser (EDS) at the NORTEM laboratory of the Norwegian
188 University of Science and Technology. After the structural characterisation of the BFS, and
189 the identification of the K-bearing phases, all grain size fractions were dated by K-Ar
190 technique. Readers are referred to Appendix for further details on the analytical procedure.

191 **4. Results**

192 **4.1 Fault anatomy and sample location**

193 The LGF is a composite brittle structure defined by a 1-1.5 m thick fault core and an up to
194 200 m thick asymmetric damage zone. The damage zone is mainly composed of grey-pale
195 green cohesive cataclasite and is thicker in the hanging wall. A dense and complex
196 network of 1-3 cm thick epidote and quartz veins cuts across the hanging wall (Fig. 2a),

197 but is not present in the immediate proximity of- and within the fault core. Towards the
198 upper part of the hanging wall, metasyenite and metamonzogranite are exposed. In the
199 footwall mylonites, the damage zone is up to 30 m thick.

200 The fault core is a tabular structure containing a principal slip surface that dips 35° to the
201 NW and bears W-plunging slickenlines (Fig. 1b). It is defined by a laterally continuous and
202 only a few mm thick smear of dark gouge (Fig. 1d). Secondary slip surfaces, subparallel to
203 the principal slip surface, occur above and below it, bounding the fault core (Figs. 1b, c).
204 They contain two sets of lineations, defined by NW- and W- plunging slickenlines (Figs. 1b,
205 2b). Riedel shears and bookshelf structures (Figs. 2e, f), together with the bending of
206 foliated gouge and sigmoidal lenses of indurated cataclasite (Figs. 2c, d), are consistent
207 with a normal top-to-the-NW sense of shear. The principal slip surface cuts across all other
208 structural features (Fig. 1d), indicating that its sinistral transtensional W-directed
209 kinematics is related to the youngest recorded increment of faulting.

210 The fault core contains juxtaposed discrete brittle domains delimited by sharp boundaries,
211 each corresponding to one of the identified BSF of the LGF (Fig. 1d). Every BSF contains
212 a distinct fault rock type, each characterised by a different degree of consolidation, colour,
213 clay content (with various degrees of plasticity in hand specimen) and geometric
214 relationships. Five BSF (BSF I to BSF V) were recognised at the outcrop (Fig. 1d) and
215 sampled for mineralogical characterisation and K-Ar dating.

216 Crosscutting relationships at the outcrop allowed to define the relative temporal sequence
217 of BSF formation, from the oldest (BSF I) to the youngest (BSF V). The fault core contains
218 competent and internally fractured lenses of a dark reddish grey indurated gouge (BSF I,
219 Fig. 3a) preserved all along a tabular domain in the central portion of the core. These
220 lenses are a few to tens of cm long and locally exhibit sigmoidal shapes (Fig. 2d). They are
221 embedded within two other brittle structural facies: a poorly consolidated cataclasite (BSF

222 II) and a weakly foliated gouge (BSF III, Fig. 1d). BSF II defines the most external portion
223 of the core and is formed by a poorly consolidated pale green cataclasite (Fig. 3b). It is the
224 most abundant structural facies in the fault core. Inside the green cataclasite there occur
225 smaller sigmoidal lenses of whitish cataclasite (identical in thin section to the greenish
226 cataclasite of BSF II), whose asymmetric shape suggests top-to-the-NW extensional
227 shearing (Figs. 1d, 2c). The green cataclasite is cut across by narrowly spaced,
228 subvertical, NNE-SSW striking fractures with sporadic calcite coatings. These subvertical
229 fractures are found exclusively within this cataclastic BSF and do not crosscut the younger
230 gouges (BSF III, IV and V). The fine-grained, weakly foliated greenish gouge (BSF III, Fig.
231 3c) cuts the green cataclasite (BSF II) and the associated system of fractures.

232 White, undulating zeolite veins are sub-parallel to the principal slip surface (Fig. 2f). These
233 veins are spatially associated with the dark reddish grey gouge (BSF I), cutting the lenses
234 thereof and the weakly foliated gouge around it (BSF III). Both lenses and veins are, in
235 turn, crosscut by sub-vertical fractures, whose geometrical arrangement is consistent with
236 top-to-the-NW extensional shearing.

237 Two other distinct types of clay-rich gouge occur in the inner part of the core. A green-grey
238 and plastic gouge variety is preserved exclusively at the north-western exposed
239 termination of the fault, geometrically below the principal slip surface (BSF IV, Fig. 3d).
240 Finally, the BSF V is represented by the smear of dark, clay-rich gouge along the principal
241 slip surface (Fig. 3e), which forms a laterally continuous 2-3 mm-thick layer and cuts all the
242 BSF described above (Fig. 3f).

243 **4.2 Microstructural analysis**

244 The damage zone in the hanging wall is mainly composed of proto-cataclastic to
245 ultracataclastic rocks (Fig. 4b). They are formed at the expense of a mylonitic gneiss (Fig.

246 4a) made of quartz-feldspar ribbons wrapped around by chlorite and epidote-rich layers
247 along the foliation (Figs. 4a, b). Quartz grains in the mylonitic domains are a few to tens of
248 μm in size, have lobate boundaries and diffuse undulose extinction. Feldspars are
249 commonly altered to sericite. Relict nuclei of K-feldspar with exsolution lamellae occur in
250 the centre of sigmoidal lithons, embedded within the foliation (Fig. 4a). An early generation
251 of coarse epidote is overprinted by a subsequent finer-grained generation. The evidence of
252 brittle deformation intensifies toward the core as documented by increased fracture density
253 and the occurrence of discrete gouge levels composed of fine-grained epidote, clay and
254 opaque minerals (Fig. 4b).

255 Rocks in the fault core form a heterogeneous fault rock assemblage from a microstructural
256 point of view. The dark reddish grey indurated gouge (BSF I) is mainly composed of
257 ultrafine-grained feldspar and clay minerals. Additionally, it exhibits rounded glassy and
258 microcrystalline domains, containing spherulites varying in diameter from 5 to 10 μm (Fig.
259 4c). Consistent with the common interpretation of spherulites as diagnostic textures of
260 frictional melts (e.g., Lin, 1994, Di Toro and Pennacchioni, 2004), we interpret these
261 domains as heavily reworked and transposed clasts of pseudotachylyte veins, now
262 preserved in the reddish gouge (BSF I).

263 The pale green cataclasite (BSF II), which forms the thickest portion of the LGF core, is
264 composed of different domains and types of clasts (Figs. 4d, e). These clasts are
265 embedded within an ultracataclastic and locally weakly foliated matrix (Fig. 4e) consisting
266 of plagioclase, quartz, epidote, smectite and titanite. All clasts are invariably cut by Fe-
267 chlorite and K-feldspar veins (Fig. 4f), themselves transposed and reworked in the
268 ultracataclastic matrix. Some clasts are foliated and made of tightly spaced bands
269 enriched in quartz and feldspars alternated with epidote-rich layers (Fig. 4d). The foliation

270 in these clasts and the evidence of crystal-plastic deformation suggest that they are
271 derived from the host rock mylonite.

272 Other clasts within the pale green cataclasite are, instead, remnants of earlier generations
273 of brittle fault rocks. Dark reddish, very fine-grained clasts are interpreted to be derived
274 from BSF I. Some clasts in the pale green cataclasite, moreover, contain a fine-grained
275 matrix embedding variably sized, reworked sub-rounded quartz and plagioclase (Figs. 4d,
276 f). Tiny K-feldspars, smectite, smectite-illite, plagioclase, apatite, quartz, oxides and Fe-
277 sulphides form the matrix (Figs. 4d, f).

278 1 to 5 mm-thick zeolite veins cut across the fault core (BSF I, II and III) but are absent in
279 the gouges along the principal slip surface. Zeolite forms either euhedral or stretched
280 fibres elongated perpendicular or at high angle to the vein walls. Randomly oriented
281 laumontite crystals are found in dilatant domains around angular clasts of earlier
282 generations of fault rocks (Fig. 4g).

283 Vertical and sub-vertical calcite veins strike NE-SW and have a variable thickness
284 between 10 μm and a few mm. Fibrous calcite crystals are oriented WSW-ENE/W-E, at
285 high angle to the vein boundaries (Fig. 4h). In some veins, they exhibit tabular, thin twins
286 (type I), indicating deformation temperatures $<200\text{ }^{\circ}\text{C}$ (Ferrill et al., 2004). A second
287 episode of calcite crystallisation occurred after the formation of the zeolite veins, i.e., after
288 the formation of the weakly foliated gouge (BSF III), and before the last slip event along
289 the principal slip surface.

290 In summary, microstructural observations constrain an increasing intensity of brittle
291 deformation toward the LGF core. Mylonite- and different generations of reworked
292 cataclasite/gouge clasts indicate a polyphase deformation history. Clasts of

293 pseudotachylyte reworked within the indurated fault gouge prove the coseismic character
294 of at least one of the early deformation events.

295 Microstructural analysis and the observed crosscutting relationships permit constraining
296 the following temporal sequence of veining, from old to young: 1) Pervasive chaotic
297 system of epidote and quartz veins within the damage zone (Fig. 2a). Fault rocks of the
298 LGF core contain fractured and transposed lenses of these epidote-rich domains.; 2)
299 Chlorite and feldspar-rich veins cutting across an early generation of fault gouge, now only
300 preserved as clasts in the fault core rocks (Fig. 4f); 3) Calcite and zeolite veins not
301 affecting the youngest generations of unconsolidated clay-rich gouge (BSF IV and V), and
302 thus predating the last stages of LGF slip (see below).

303 **4.3 Fault rock compositional data**

304 Samples from all the studied BSF have different mineralogical compositions. The relative
305 abundance of mineral phases varies with grain size within the same sample. K-feldspar,
306 epidote, chlorite and smectite occur in all structural facies (Table 1). XRD analysis
307 documents a gradual increase of clay minerals towards the finest fractions from a
308 minimum of 4 to a maximum of 44 wt% in the 0.1-0.4 μm fractions (e.g., in BSF V the
309 concentration of clay minerals quadruples, Fig. 5e). The most abundant clay minerals in
310 the fault core are smectite and illite. TEM analysis confirms the presence of K-bearing
311 phases also in the finest fractions where we could not carry out XRD analysis due to the
312 lack of sufficient material. Illite, mostly Fe-illite, smectite and K-smectite were detected in
313 $<0.1 \mu\text{m}$ grain size fraction (Figs. 5a-c). K-feldspar is an additional K-bearing phase that is
314 present in all grain size fractions of all samples. At the TEM, euhedral K-feldspar crystals
315 have been documented to also occur in the $<0.1 \mu\text{m}$ fraction of BSF I to IV (Fig. 5d). XRD
316 and TEM analysis do not document illite in any grain size fractions of BSF III, which,
317 instead, contains smectite and K-feldspar.

318 In all samples, except that from BSF II, the percentage of K-feldspar decreases towards
319 the finer grain size fractions (Fig. 5). In BSF I, K-feldspar ranges between 50 wt% in the
320 coarser- and 30 wt% in the 0.1-0.4 μm grain size fraction. Similarly, the most clay-rich
321 gouges (BSF IV and V) contain relatively high amounts of K-feldspar, which is still between
322 27 and 22 wt% in the finest fractions (Fig. 5e).

323 Chlorite is present in all dated fractions and its content tends to increase with decreasing
324 grain size. Plagioclase is not ubiquitous in the samples, but it is one of the main
325 components in BSF II and III. Epidote is a common phase in all BSF, but its content
326 generally decreases with decreasing grain size. It is very abundant (c. 45 wt%) in the
327 foliated greenish gouge of BSF III. Quartz is only sporadically found in BSF III, IV and V,
328 and its concentration decreases steadily with grain size. Two zeolite types occur with
329 different relative abundance, stilbite and laumontite (Table 1). Pyroxene does not exceed
330 6% and it is absent in BSF IV and V. Calcite occurs as an accessory phase.

331 In summary, the general trend of decreasing quartz, epidote and K-feldspar contents in the
332 finer grain-size fractions (0.1-0.4 and 0.4-2 μm) is compensated by the increase of illite,
333 smectite and chlorite. This trend suggests that quartz and epidote are protolithic minerals
334 that did not crystallise during deformation. Pyroxene is a high temperature phase, and is
335 thus considered to be inherited in all BSF. The euhedral habit of K-feldspar in the <0.1 μm
336 grain size fraction (Fig. 5d), however, allows us to deduce that K-feldspar also grew
337 authigenically during faulting. Moreover, the presence of zeolites in BSF I, II and III, which
338 correspond to the most competent rocks in the fault core, allows us to constrain a
339 maximum deformation temperature during faulting of c. 200 °C (Weisenberger and Bucher,
340 2010). At that temperature, K-feldspar is indeed capable to grow authigenically and
341 sinkinematicly (Mark et al., 2008; Sasseville et al., 2008; Brockamp and Clauer, 2013).

342 **4.4 K-Ar radiometric data**

343 K-Ar ages range from 195 ± 4 Ma to 57 ± 1 Ma (Table 2). “Radiometrically determined age
344 vs. grain size” plots of the dated samples define inclined curves (Fig. 6), where the finest
345 grain size fractions yield invariably the youngest ages, and the coarsest fractions (2-6, 6-
346 10 μm) yield the oldest. All the ten ages of the 2-6 and 6-10 μm fractions define a cluster
347 with a mean age of 179 ± 2 Ma (MSWD=7.4). The ages of the <0.1 μm fraction are $121 \pm$
348 3 , 87 ± 2 , 78 ± 2 Ma, and 57 ± 1 Ma. BSF I yielded the oldest <0.1 μm K-Ar age of 121 ± 3
349 Ma; its coarsest grain size fraction (6-10 μm) yielded an age of 186 ± 4 Ma. The weakly
350 foliated gouge yielded dates between 87 ± 2 Ma for the <0.1 μm fraction, and of 167 ± 3
351 Ma for the 6-10 μm . The greenish clay-rich gouge, yielded dates between 78 ± 2 Ma and
352 184 ± 4 Ma for the <0.1 and 6-10 μm fractions, respectively. In BSF V, the <0.1 μm
353 fraction yielded the youngest age of the entire dataset at 57 ± 1 Ma.

354 For the greenish cataclasite (BSF II) we could not date the <0.1 μm fraction; the 0.1-0.4
355 μm fraction yielded a date of 132 ± 3 Ma, which progressively increases towards the 6-10
356 μm fraction and represents the oldest age of the entire dataset at 195 ± 4 Ma. In the “age
357 vs. grain size fraction” diagram of Fig. 6 the pale green line referring to BSF II can be
358 traced between 121 and 87 Ma for the finest grain size. This age extrapolation does not
359 follow any analytical constraints. The meso- and microstructural data from BSF II and the
360 crosscutting relationships with the other structural facies allow us to conclude that the pale
361 green cataclasite could be of Late Cretaceous age, i.e., an age between the formation of
362 the reddish indurated- (BSF I) and of the weakly foliated gouge (BSF III).

363 **5. Discussion**

364 **5.1 Interpretations of the new K-Ar dates**

365 The “age vs. grain size” curves obtained during this study (Fig. 6) are conceptually
366 identical to those produced by other K-Ar geochronological studies of fault-related rocks
367 (Pevear, 1999; Zwingmann and Mancktelow, 2004; Bense et al., 2013; Davids et al., 2013;

368 Yamasaki et al., 2013; Torgersen et al., 2015a; Viola et al., 2016; Aldega et al., 2019).
369 Such inclined curves are generally interpreted as recording variable contamination of the
370 authigenic and synkinematic mineral phase separates by inherited protolithic minerals,
371 mixing of different generations of authigenic minerals, and grain-size-dependent ^{40}Ar loss
372 (van der Pluijm et al., 2001; Verdel et al., 2012; Torgersen et al., 2015a, b; Viola et al.,
373 2016, Vrolijk et al., 2018).

374 Since brittle faulting is dilatational and may thus enhance the ingress of fluids into the
375 actively deforming rock volume, synkinematic formation of new phases and/or
376 recrystallisation of pre-existing minerals (or parts thereof) is common (Haines and van der
377 Pluijm, 2008; Tagami, 2012; Vrolijk et al., 2018). Newly crystallised minerals will be the
378 most abundant in the finer grain size fractions. Even the finest grain size fractions,
379 however, may still include inherited protolithic minerals or different generations of
380 authigenic phases reworked during multiple stages of deformation. Ages obtained from the
381 finest grain size fractions should thus be still considered as maximum ages, although they
382 provide the best available constraint on the timing of the most recent faulting event the
383 rock recorded (van der Pluijm et al., 2001; Zwingmann and Mancktelow, 2004; Torgersen
384 et al., 2015b; Viola et al., 2016).

385 The coarser grain size fractions, on the contrary, are enriched in protolithic (inherited)
386 minerals, such as, for example, older generations of K-feldspar. If the coarser grain sizes
387 of different samples from one single fault zone yield the same age, it is reasonable to
388 conclude that they constrain a common thermal or faulting event. Such an early event
389 likely occurred at higher temperature than the more recent ones recorded by the finer
390 fractions (e.g., Viola et al., 2016; Vrolijk et al., 2018; Scheiber et al., 2019). The
391 intermediate grain size fractions (0.4-2 and 2-6 μm) generally define a trend of decreasing
392 age with decreasing grain size, as they result from the mixing of different (synkinematic

393 and protolithic) grains with varying isotopic signatures and are, therefore, commonly
394 devoid of a real geological meaning.

395 In agreement with our compositional data, we adopt the Age Attractor Model (Torgersen et
396 al., 2015a, b; Viola et al., 2016) and thus rely on the concept of progressively increasing
397 amounts of authigenic and synkinematic K-bearing phases with decreasing grain size,
398 such that we consider the finest fractions as mainly composed of authigenic, synkinematic
399 minerals.

400 In this study, the ages of all BSF of the fault core span the c. 195 to 57 Ma time interval.
401 Interestingly, there are no ages older than 195 ± 4 Ma (Jurassic). The Jurassic mean age
402 of 179 ± 2 Ma calculated from all the 2-6 and 6-10 μm grain size fractions cannot be
403 related to the age of the host rock, because the youngest host rock in Lærdal is Cambrian
404 (Milnes and Corfu, 2011; Corfu et al., 2014). The c. 180 Ma age might, therefore, be
405 interpreted as resulting from a major deformation event and be related to the initiation of
406 brittle faulting along the LGF. The Jurassic and Early Cretaceous activity of the LGF was
407 already constrained by previous authors by different dating techniques (Andersen et al.,
408 1999; Fossen et al., 2016). Our obtained range of ages is comparable with results of
409 Fossen et al. (2016), who documented ages between 191 and 64 Ma for the 2-6 μm and
410 <0.2 μm fractions from the fault core of the LGF. From the common Jurassic age cluster of
411 Fig. 6, each dated BSF follows a different “age vs. grain size” path. Post-Jurassic
412 deformation and/or fluid ingress did thus not cause pervasive illite recrystallisation up to
413 the coarsest fractions, which still yield their original Jurassic age, but instead synkinematic
414 growth of illite up to the <2 μm grain size fractions. These results document therefore the
415 evolution of rocks, which, from a single initial radiometric signature recorded at higher
416 temperature, responded differentially during several later episodes of deformation. In fact,

each BSF tracks one of the subsequent deformation events with their specific compositional, structural and isotopic signatures (see Viola et al., 2016, their Fig. 5).

The K-Ar dating approach to brittle faults is generally applied on clays separated from fault rocks (van der Pluijm et al., 2001; Zwingmann and Mancktelow, 2004; Tagami, 2012; Vrolijk et al., 2018). TEM analysis is crucial to identify all K-bearing phases present in the finest fractions, such as illite, smectite and K-feldspar as they could either be simply inherited from the host rock and isotopically reset during faulting or be of authigenic, synkinematic origin (Mark et al., 2008; Sasseville et al., 2008; Surace et al., 2011; Torgersen et al., 2015b). Microstructural, compositional, and thermochronological data from the LGF suggest that the temperature did not exceed 200 °C during the Cretaceous (Ferrill et al., 2004; Weisenberger and Bucher, 2010; Johannessen et al., 2013). The Ar closure temperature for 1 µm illite/muscovite and K-feldspar grains is generally c. 210-250°C (Kelley, 2002; Verdel et al., 2012; Torgersen et al., 2015a). Thus, thermally induced volume diffusion effects, which could have reset the isotopic clock of the finest grain size fractions, are not considered in our interpretative model. Moreover, TEM images document the presence of authigenic Late Cretaceous K-feldspar, proving that it is indeed a synkinematic phase in the finest grain size fractions (see Torgersen et al., 2015a).

5.2 Fault evolution

In order to reconstruct the LGF evolution, being able to assign a K-Ar date to each recognised BSF allows us to correlate the age of K-bearing mineral authigenesis with a specific brittle deformation event. Microstructural observations indicate that the LGF grew in response to widespread cataclastic flow and fracturing superposed on an earlier ductile precursor. The presence of mylonite clasts and multiple generations of cataclasite/gouge support the interpretation of a polyphase deformation history. Additionally, the different

441 composition of each BSF suggests that the LGF has deformed different lithologies and
442 units during its multiple reactivations.

443 In the following, we deconvolve the LGF deformation history and propose a time-
444 constrained conceptual model for the fault (Fig. 7). The brittle fault partially reworked a
445 precursor ductile shear zone (Fig. 7a). Deformation was likely associated with diffuse
446 seismicity, generating pseudotachylytes. Crustal-scale extension caused the exhumation
447 of deep crustal blocks and their progressive transition, while en-route to the surface, to
448 colder and shallower conditions. Syndeformational fluid circulation created a pervasive
449 network of epidote and quartz veins cutting through the mylonites and the proto-cataclasite
450 that, by then, had formed mainly at the expense of the hanging wall sequence (Fig. 7a).
451 Cross-cutting relationships visible at the outcrop permit to conclude that the c. 121 Ma old
452 dark reddish grey and indurated gouge (BSF I) represents the oldest BSF preserved in the
453 fault core. Its composition, with up to 50% K-feldspar in the coarsest grain size fraction,
454 suggests that it formed at the expense of a K-feldspar-rich rock. Deformation and the
455 ingress of fluid allowed the crystallisation of a clay-rich gouge with smectite, illite and
456 chlorite, also embedding clasts of reworked pseudotachylyte (Fig. 7b). The remarkable
457 hardness of the preserved lenses of this gouge, compared to the surrounding parts of the
458 fault core, could be due to early induration processes by, for example, zeolite
459 crystallisation (Table 1, Fig. 4g, Olsen et al., 1998). The early induration likely induced
460 mechanical hardening of the fault core, requiring further deformation to affect a
461 progressively wider volume of the rock by propagating into the hanging wall and footwall
462 mylonites (Fig. 7c). A renewed episode of deformation formed the pale green cataclasite
463 (BSF II), composed of heterogeneous clasts of older fault rocks (Fig. 7c). The finest grain
464 size fraction ($<0.1\ \mu\text{m}$) of the pale green cataclasite contained insufficient material for K-Ar
465 analysis, but relative chronological constraints at the outcrop and microstructural evidence
466 suggest that this BSF formed in the Late Cretaceous (Fig. 6, see Section 4.4). This BSF is

467 cut by NNE-SSW striking fractures, locally filled with calcite. The orientation of these
468 fractures and veins constrain WNW-ESE extension, which is in agreement with the
469 dominant normal kinematics of the fault. These fractures do not crosscut the younger
470 gouges (BSF III, IV and V), indicating that BSF III to V post-date fracturing and the
471 associated early calcite veining.

472 At c. 87 Ma a weakly foliated gouge formed in the centre of the fault core (BSF III, Fig. 7d).
473 This Cretaceous and the following episodes of slip, up to the probable locking and healing
474 of LGF at c. 57 Ma, were characterised by the narrowing of the active deformation zone.
475 Fault narrowing was likely due to the progressive accumulation of clays in the core, and to
476 the decreasing deformation temperature (Rutter et al., 2001; Scheiber et al., 2019). Slip
477 was accommodated by the formation of a weakly foliated gouge and by the nucleation of
478 Riedel shears in the consolidated fault facies (BSF I and II). BSF II and III contain
479 plagioclase, K-feldspar and pyroxene, such that they probably derive from a mangeritic
480 protolith of the Jotun Nappe Complex (Milnes and Corfu, 2011; Corfu et al., 2014).
481 Interestingly, the foliated gouge of BSF III does not contain illite but smectite and K-
482 feldspar. Almost identical amounts of K-feldspar are documented in all grain size fractions
483 (c. 9-10%), because of its relative enrichment due to synkinematic neoblastesis.

484 In agreement with the discussed scenario of decreasing temperature through time, the
485 progressive evolution of the fault caused the formation of unconsolidated, extremely
486 localised fault gouges (BSF IV and V) in the centre of the core. BSF IV and V are distinctly
487 different from the older brittle facies as they include significant amounts of smectite and
488 illite. A green-grey gouge enriched in synkinematic illite, smectite and chlorite formed at 78
489 Ma (Fig. 7e). Finally, a thin, laterally continuous smear of dark gouge cut across all BSF,
490 constraining a last transtensional top-to-the-W increment of faulting of the LGF at 57 Ma
491 (Fig. 7f). The likely very low permeability of clay-rich gouge (Evans et al., 1997; Faulkner

492 and Rutter, 2003) suggests that crystallisation of illite and smectite occurred during faulting
493 and not during post-deformational alteration. There is no evidence of other significant
494 deformation episodes affecting the Paleogene clay-rich smear, and we conclude that the
495 LGF ceased its (recorded) activity c. 57 Ma ago.

496 **5.3 Regional implications**

497 Our new dataset has also implications for the regional geological framework. The obtained
498 LGF geochronological results do not record any evidence of fault activity prior to the
499 Jurassic (Table 2), questioning whether this fault is indeed a Devonian structure (Corfu et
500 al., 2014; Fossen et al., 2016). Lack of Palaeozoic ages in the studied BSF could be due
501 to (1) selective sampling that would have missed potential pre-Jurassic domains, (2) Ar-
502 loss or thermal effects or (3) obliteration of any pre-Jurassic isotopic signal in all grain size
503 fractions. Our structural characterisation, however, was detailed and thorough and we
504 sampled all BSF recognised at the main LGF outcrop. The LGF, however, is a very long
505 brittle structure (Andersen et al., 1999) and we cannot exclude the possibility that Pre-
506 Jurassic ages, if present, may be preserved elsewhere along the fault strike. Ar-loss or
507 thermal effects can be considered unlikely in a system that underwent progressive cooling
508 to below 250 °C from the Devonian onwards (Johannessen et al., 2013; Walsh et al.,
509 2013; Ksienzyk et al., 2014, 2016 and references therein). As previous studies
510 demonstrate, even in very highly-strained and multiply activated faults, earlier slip events
511 are not completely obliterated, and they may be resolved by K-Ar dating of the coarser
512 grain size fractions (Viola et al., 2016). As a consequence, Devonian to pre-Jurassic K-Ar
513 ages, if ever present, would have most probably been preserved in the fault and detected
514 during this study (cf. Torgersen et al, 2015). However, if the brittle LGF did accommodate
515 a Palaeozoic history, it is likely that the structural and isotopic evidence thereof is

516 preserved only in the cohesive cataclasites and proto-cataclasites of the damage zone,
517 which we did not date, and not in the fault core (e.g., Scheiber et al., 2019).

518 The LGF preserves evidence of at least five geological significant (re)activation episodes
519 (from the Jurassic to the Paleogene), with indications of coseismic rupturing.
520 Pseudotachylyte developed likely during the Jurassic or the possible earlier localisation
521 history of the LGF. The oldest recorded event at c. 180 Ma could represent crustal
522 stretching associated with the second phase of the North Sea rifting (Gabrielsen et al.,
523 1999; Fossen et al., 2016; Viola et al., 2016). The Cretaceous events at c. 121, 87 and 78
524 Ma can be related to the hyperextension accommodation along the Mid-Norwegian margin
525 during progressive cooling and exhumation (cf. Fossen et al., 2016; Ksienzyk et al., 2016;
526 Scheiber and Viola, 2018). The last recorded Paleogene event (c. 57 Ma), documented by
527 the laterally continuous clay smear along the principal slip surface, likely sealed the fault.
528 The tectonic phase expressed by this geological feature remains, however, poorly
529 constrained, even though other K-Ar Paleogene faulting ages are reported from
530 southwestern Norway (Fossen et al., 2016; Scheiber et al., 2019).

531 **6. Conclusion**

532 We have presented a methodological approach that is of general validity and that can aid
533 when reading geological archives stored in brittle faults. The present-day LGF core
534 exposes the tight juxtaposition of several BSF. Each BSF is defined by specific fault rocks
535 and is characterised by a unique isotopic signature, fully resolvable by K-Ar
536 geochronology. This study also confirms that extreme localisation of strain, associated with
537 synkinematic (re)crystallisation is indeed a common process within brittle faults (cf.
538 Torgersen et al., 2015a; Viola et al., 2016; Scheiber et al., 2019). The concept of BSF can
539 thus be very useful when characterising complex faults, because BSF can help resolve the
540 spatial and temporal deformation history of fault zones in multiply deformed bedrock

541 terranes, which have experienced both ductile and brittle deformation. Additionally, BSF
542 can be an important tool to investigate and constrain in time the diachronic and
543 heterogeneous evolution of fault cores.

544 **Acknowledgments**

545 This paper presents some of the results obtained during the BASE project (“Basement
546 fracturing and weathering onshore and offshore Norway—Genesis, age, and landscape
547 development”), a research initiative launched and steered by the Geological Survey of
548 Norway (NGU) and funded by Det Norske Oljeselskap (now Aker BP ASA), Lundin
549 Petroleum, Maersk Oil, Wintershall, and the NGU. The paper finalisation took place during
550 the BASE 2 project supported by Equinor, Aker BP, NPD, Lundin, Spirit Energy,
551 Wintershall and NGU. TEM work was carried out using the NORTEM infrastructure at the
552 TEM Gemini Centre of the Norwegian University of Science and Technology (NTNU),
553 Norway. Ruikai Xie at the Geological Survey of Norway is thanked for performing K
554 analyses. We thank all BASE colleagues for continuous discussion and constructive
555 inputs. Laurel Goodwin and an anonymous reviewer are thanked for having greatly
556 improved the initial version of this paper.

557

558 *Figure 1: a) Simplified geological map of southwestern Norway with the main structural*
559 *features of the area. Black star: Lærdal study site; b) Schmidt projection (lower*
560 *hemisphere) of the principal and secondary slip surfaces of the fault and their associated*
561 *striae. The black arrows show the direction of slip of the hanging wall; c) detailed view to*
562 *the southwest of the studied LGF outcrop. The principal slip surface (red dashed line) is*
563 *represented by a thin, laterally continuous smear of dark gouge, while two subparallel*
564 *secondary slip surfaces (yellow dashed lines) frame the fault core. Stars indicate sample*

565 locations. All samples were dated by K-Ar. A 40 cm long hammer for scale in the lower
566 part of the outcrop; d) simplified scheme of the BSF of the fault core.

567 Figure 2: Structural features of the LGF. a) Cm-thick epidote and quartz vein cutting
568 across the hanging wall monzogranite; b) upper secondary slip surface. The red lines
569 represent the direction of slip of the missing block, i.e., the footwall, according to the
570 slickenlines; c) white sigmoidal lenses of cataclasite embedded by the pale green
571 cataclasite (BSF II) constraining a top-to-the-NW sense of shear; d) top-to-the-NW
572 sigmoidal lens of dark reddish grey indurated gouge (BSF I) embedded within a weakly
573 foliated gouge (BSF III); e) extensional top-to-the-NW bookshelf structures within dark
574 competent reddish grey gouge (BSF I); f) lens of dark reddish grey indurated gouge (BSF
575 I) cut by Riedel fractures. Both the reddish gouge and the host fault rock contain white,
576 undulate zeolite veins subparallel to the principal slip surface, marked by yellow arrows.

577 Figure 3: Different brittle structural facies of the fault core and their representative samples
578 for K-Ar dating. The colours of the labels from “a” to “e” are the same of Fig. 2. a) BSF I,
579 lens of dark reddish grey indurated gouge; b) BSF II, pale green cataclastic brittle domain
580 representing the most common portion of the fault core; c) BSF III, green, weakly foliated
581 gouge embedding a lithon of BSF I; d) BSF IV, clay-rich gouge preserved just below the
582 principal slip surface of “e” and “f”; e) BSF V, dark smear of black gouge representing a
583 laterally continuous, only a few mm-thick layer along the principal slip surface (f).

584 Figure 4: Microphotographs of representative microstructures of the main LGF fault rocks.
585 a) View of thin section cut perpendicular to the foliation and parallel to the stretching
586 lineation. Mylonitic gneiss from the hanging wall of the LGF with quartz-feldspar domains
587 within an epidote and chlorite-defined foliation. A feldspar sigmoidal lens indicates simple
588 shear deformation; b) cataclasite, enriched in epidote, resulting from the hanging wall
589 protolith; note widespread fracturing and the presence of poorly sorted, angular clasts; c-h)

590 views of thin sections cut perpendicular to the fault and parallel to slickenlines; c) SEM
591 image of clasts (in yellow) of spherulites (in white) in a fault gouge matrix, representing
592 heavily transposed and recrystallised pseudotachylyte fragments; d) SEM image of clasts
593 of different fault rock domains and mylonites (in yellow) embedded within an
594 ultracataclastic matrix within the pale green cataclasite (BSF II); e) microphotograph of the
595 same ultracataclastic matrix of (d) with flow structures; f) SEM image of a gouge clast in
596 BSF II made of feldspars, smectite, quartz and oxides. The clast is cut by Fe-chlorite and
597 K-feldspar veins; g) laumontite crystals around clasts of an early generation of indurated
598 fault gouge; h) fibrous calcite veins parallel to the NW-SE striae. Mineral abbreviations
599 after Whitney and Evans (2010).

600 Figure 5: Mineralogical composition of each BSF. a-d) Photos and EDS spectra of K-
601 bearing phases in the $<0.1\ \mu\text{m}$ fraction by TEM analysis; e) XRD compositional data for
602 each of the studied fractions.

603 Figure 6: K-Ar age vs. grain size diagram, showing inclined age curves for all samples. A
604 mean age of $c. 179 \pm 2\ \text{Ma}$ is computed for the two coarsest fractions of all samples,
605 highlighted by the light blue bar.

606 Figure 7: Conceptual model of LGF evolution through time. a) Pseudotachylyte formed
607 during coseismic rupturing, and an earlier fault zone formed at the expense of a mylonitic
608 shear zone. Fluid infiltration created a network of epidote and quartz veins; b) deformation
609 and fluid ingress led to the formation of a dark reddish grey, indurated gouge and caused
610 overall strengthening of the fault core. The gouge embeds clasts of pseudotachylyte; a
611 fracture-rich damage zone (DZ) formed; c) renewed cataclasis affected the previously
612 formed BSF and the host rock leading to the widening of the active fault zone and the
613 formation of the pale green cataclastic facies in the Late Cretaceous; d) at $c. 87\ \text{Ma}$ a
614 weakly foliated gouge developed in the inner part of the fault core, leading to the

615 progressive narrowing of the active zone; e) extreme localisation led to the formation of a
616 green-grey gouge highly enriched in clay minerals; f) a thin, laterally continuous smear of
617 dark gouge cut across all the other BSF, accommodating a last transtensional top-to-the-
618 W increment of faulting at c. 57 Ma.

619 Table 1: XRD data. Mineral concentrations are given in wt%. GOF represents “Goodness
620 of Fit”. “x”: unquantified amount.

Sample	Size fraction [µm]	Quartz	K-feldspar	Plagioclase	Illite/Muscovite	Chlorite	Smectite	Stilbite	Laumontite	Heulandite	Epidote	Pyroxene	Calcite	GOF
BSF I	0.1-0.4	-	30	-	-	32	26	-	2	-	4	6	trace?	1.76
	0.4-2	-	40	-	-	27	18	-	2	-	7	6	trace?	1.51
	2-6	-	47	-	-	23	13	-	2	-	10	5	trace?	1.47
	6-10	-	50	trace	-	22	12	-	2	-	9	4	1	1.43
BSF II	0.4-2	-	12	30	trace?	20	8	4	6	trace	16	4	-	1.51
	2-6	-	11	26	-	10	5	8	17	trace	20	3	-	1.46
	6-10	-	10	24	-	8	4	12	21	trace	18	3	-	1.47
BSF III	<0.1	<0.1	-	-	-	x?	x	x	-	-	-	x	x	-
	0.1-0.4	-	9	10	-	36	22	-	trace	-	18	5	-	1.65
	0.4-2	trace	9	17	-	15	11	-	trace	-	43	4	1	1.43
	2-6	1	9	17	-	12	9	-	2	-	45	4	1	1.41
	6-10	1	10	20	-	12	8	-	2	-	42	3	2	1.38
BSF IV	<0.1	-	x	-	x	x	x	-	-	-	x	-	-	-
	0.1-0.4	2	22	-	14	21	29	-	-	-	8	-	3	1.56
	0.4-2	4	33	-	15	13	20	-	-	-	13	-	2	1.42
	2-6	11	37	-	5	11	16	-	-	-	19	-	1	1.37
	6-10	14	35	-	4	11	15	-	-	-	19	-	2	1.35
BSF V	0.1-0.4	-	27	4	30	21	14	-	-	-	4	-	-	1.4
	0.4-2	-	25	5	30	20	15	-	-	-	5	-	-	1.4
	2-6	6	38	6	8	8	5	1	trace	-	28	-	-	1.34
	6-10	7	39	5	5	9	7	1	2	-	25	-	-	1.35

621

622 Table 2: K-Ar radiometric data and ages for each grain size fraction of the samples.

Sample Parameters			⁴⁰ Ar*			K		Age Data	
Sample	Size fraction [µm]	Mass [mg]	⁴⁰ Ar* [mol/g]	σ [%]	⁴⁰ Ar* [%]	K [wt %]	σ [%]	Age [Ma]	σ [Ma]
BSF I	<0.1	0.72	2.73E-10	0.99	62.1	1.261	2.00	120.8	2.7
	0.1-0.4	2.50	6.58E-10	0.34	87.8	2.452	2.00	148.5	3.0
	0.4-2	3.25	1.18E-09	0.31	92.5	3.877	2.00	168.1	3.4
	4-6	4.36	1.58E-09	0.30	97.8	4.685	2.00	184.8	3.7
	6-10	3.73	1.76E-09	0.31	98.5	5.171	2.00	186.3	3.8
BSF II	0.1-0.4	1.92	2.44E-10	0.48	93.6	1.028	2.00	132.0	2.7
	0.4-2	2.23	3.95E-10	0.38	78.4	1.356	2.00	160.7	3.3
	4-6	7.56	4.51E-10	0.29	96.3	1.324	2.00	186.4	3.8
	6-10	8.72	4.46E-10	0.29	93.9	1.250	2.00	194.9	3.9
BSF III	<0.1	2.23	4.89E-11	1.44	18.4	0.318	2.00	86.6	2.1
	0.1-0.4	3.69	1.66E-10	0.39	59.2	0.789	2.00	117.7	2.4
	0.4-2	3.30	2.77E-10	0.35	80.6	1.029	2.00	148.8	3.0
	4-6	2.04	3.45E-10	0.40	86.1	1.031	2.00	183.2	3.7
	6-10	3.39	3.39E-10	0.34	91.2	1.119	2.00	166.8	3.4
BSF IV	<0.1	1.32	1.14E-10	1.07	20.2	0.830	2.00	77.7	1.8
	0.1-0.4	3.13	3.2E-10	0.35	57.0	1.543	2.00	115.8	2.4
	0.4-2	3.23	9.09E-10	0.31	81.4	3.071	2.00	163.0	3.3
	4-6	5.61	1.29E-09	0.29	93.6	3.927	2.00	179.8	3.6
	6-10	3.46	1.28E-09	0.31	92.1	3.793	2.00	184.3	3.7
BSF V	<0.1	1.32	1.29E-10	0.96	49.4	1.278	2.00	57.4	1.3
	0.1-0.4	1.70	4.32E-10	0.42	78.3	2.639	2.00	91.9	1.9
	0.4-2	1.79	9.99E-10	0.37	91.5	3.983	2.00	139.1	2.8

4-6	4.73	1.28E-09	0.30	97.5	4.034	2.00	174.1	3.5
6-10	2.62	1.26E-09	0.33	96.4	4.115	2.00	168.7	3.4

623

- 624 Aldega, L., Viola, G., Casas-Sainz, A., Marcén, M., Román-Berdiel, T., Lelij, R., 2019. Unravelling
625 multiple thermo-tectonic events accommodated by crustal-scale faults in northern Iberia, Spain:
626 Insights from K-Ar dating of clay gouges. *Tectonics* <https://doi.org/10.1029/2019tc005585>.
- 627 Andersen, T.B., Torsvik, T.H., Eide, A.E., Osmundsen, P.T., Faleide, J.I., 1999. Mesozoic
628 extensional faulting within the Caledonides of central south Norway. *J. Geol. Soc.* 156, 1073-1080,
- 629 Aydin, A., 2000. Fractures, faults, and hydrocarbon entrapment, migration and flow. *Marine and*
630 *Petroleum Geology* 17, 797-814,
- 631 Bense, F.A., Wemmer, K., Loebens, S., Siegesmund, S., 2013. Fault gouge analyses: K-Ar illite
632 dating, clay mineralogy and tectonic significance - A study from the Sierras Pampeanas, Argentina.
633 *Int. J. Earth Sci.* <https://doi.org/10.1007/s00531-013-0956-7>.
- 634 Braathen, A., Tveranger, J., Fossen, H., Skar, T., Cardozo, N., Sernshaug, S.E., Bastesen, E.,
635 Sverdrup, E., 2009. Fault facies and its application to sandstone reservoirs. *Aapg Bull.* 93, 891-
636 917, <https://doi.org/10.1306/03230908116>.
- 637 Brockamp, O., Clauer, N., 2013. Hydrothermal and unexpected diagenetic alteration in Permian
638 shales of the Lodève epigenetic U-deposit of southern France, traced by K-Ar illite and K-feldspar
639 dating. *Chem. Geol.* 357, 18-28, <https://doi.org/10.1016/j.chemgeo.2013.08.009>.
- 640 Caine, J.S., Evans, J.P., Forster, C.B., 1996. Fault zone architecture and permeability structure.
641 *Geology* 24, 1025-1028,
- 642 Chester, F.M., Logan, J.M., 1986. Implications for Mechanical Properties of Brittle Faults from
643 Observations of the Punchbowl Fault Zone, California. *Pure Appl. Geophys.* 124, 79-106,
- 644 Clauer, N., 2013. The K-Ar and ⁴⁰Ar/³⁹Ar methods revisited for dating fine-grained K-bearing clay
645 minerals. *Chem. Geol.* 354, 163-185, <https://doi.org/10.1016/j.chemgeo.2013.05.030>.
- 646 Corfu, F., Andersen, T.B., Gasser, D., 2014. The Scandinavian Caledonides: main features,
647 conceptual advances and critical questions. *Geol. Soc. London, Spec. Publ.* 390, 9-43,
648 <https://doi.org/10.1144/sp390.25>.
- 649 Davids, K., Wemmer, K., Zwingmann, H., Kohlmann, F., Jacobs, J., Bergh, S.G., 2013. K-Ar illite
650 and apatite fission track constraints on brittle faulting and the evolution of the northern Norwegian
651 passive margin. *Tectonophysics* 608, 196-211, <https://doi.org/10.1016/j.tecto.2013.09.035>.
- 652 Di Toro, G., Pennacchioni, G., 2004. Superheated friction-induced melts in zoned
653 pseudotachylytes within the Adamello tonalites (Italian Southern Alps). *J. Struct. Geol.* 26, 1783-
654 1801, <https://doi.org/10.1016/j.jsg.2004.03.001>.
- 655 Evans, J.P., Forster, C.B., Goddard, J.V., 1997. Permeability of fault-related rocks, and
656 implications for hydraulic structure of fault zones. *Journal of Structural Geology*, 19, 1393-1404,
- 657 Faulkner, D.R., Rutter, E.H., 2003. The effect of temperature, the nature of the pore fluid, and
658 subyield differential stress on the permeability of phyllosilicate-rich fault gouge. *Journal of*
659 *Geophysical Research: Solid Earth* 108 <https://doi.org/10.1029/2001jb001581>.
- 660 Ferrill, D.A., Morris, A.P., Evans, M.A., Burkhard, M., Groshong, R.H., Onasch, C.M., 2004. Calcite
661 twin morphology: a low-temperature deformation geothermometer. *J. Struct. Geol.* 26, 1521-1529,
662 <https://doi.org/10.1016/j.jsg.2003.11.028>.

663 Fossen, H., Dunlap, W.J., 1998. Timing and kinematics of Caledonian thrusting and extensional
664 collapse, southern Norway: Evidence from $^{40}\text{Ar}/^{39}\text{Ar}$ thermochronology. *J. Struct. Geol.* 20, 765-
665 781,

666 Fossen, H., Hurich, C.A., 2005. The Hardangerfjord Shear Zone in SW Norway and the North Sea:
667 a large-scale low-angle shear zone in the Caledonian crust. *J. Geol. Soc. London* 162, 675-687,
668 <https://doi.org/10.1144/0016-764904-136>.

669 Fossen, H., Khani, H.F., Faleide, J.I., Ksienzyk, A.K., Dunlap, W.J., 2016. Post-Caledonian
670 extension in the West Norway–northern North Sea region: the role of structural inheritance. *Geol.*
671 *Soc. London, Spec. Publ.* 439, 465-486, <https://doi.org/10.1144/sp439.6>.

672 Gabrielsen, R.H., Odinsen, T., Grunnaleite, I., 1999. Structuring of the Northern Viking Graben and
673 the More Basin; the influence of basement structural grain and the particular role of the More
674 Trondelag Fault Complex. *Marine and Petroleum Geology* 16, 443-465,

675 Haines, S.H., van der Pluijm, B.A., 2008. Clay quantification and Ar-Ar dating of synthetic and
676 natural gouge: Application to the Miocene Sierra Mazatan detachment fault, Sonora, Mexico. *J.*
677 *Struct. Geol.* 30 <https://doi.org/10.1016/j.jsq.2007.11.012>.

678 Holdsworth, R.E., 2004. Weak faults - Rotten cores. *Science* 303, 181-182,

679 Johannessen, K.C., Kohlmann, F., Ksienzyk, A.K., Dunkl, I., Jacobs, J., 2013. Tectonic evolution of
680 the SW Norwegian passive margin based on low-temperature thermochronology from the
681 innermost Hardangerfjord area. *Norw. J. Geol.* 93, 243-260,

682 Kelley, S.P., 2002. Excess argon in K–Ar and Ar–Ar geochronology. *Chem. Geol.* 188, 1-22,

683 Ksienzyk, A.K., Dunkl, I., Jacobs, J., Fossen, H., Kohlmann, F., 2014. From orogen to passive
684 margin: constraints from fission track and (U-Th)/He analyses on Mesozoic uplift and fault
685 reactivation in SW Norway., *Geol. Soc. London Spec. Publ.*

686 Ksienzyk, A.K., Wemmer, K., Jacobs, J., Fossen, H., Schomberg, A.C., Süssenberger, A.,
687 Lünsdorf, N.K., Bastesen, E., 2016. Post-Caledonian brittle deformation in the Bergen area. *Norw.*
688 *J. Geol.* 96 <https://doi.org/10.17850/njg96-3-06>.

689 Lin, A., 1994. Microlite Morphology and Chemistry in Pseudotachylite, from the Fuyun Fault Zone,
690 China. *The Journal of Geology* 102, 317-329,

691 Mark, D.F., Kelley, S.P., Lee, M.R., Parnell, J., Sherlock, S.C., Brown, D.J., 2008. Ar-Ar dating of
692 authigenic K-feldspar: Quantitative modelling of radiogenic argon-loss through subgrain boundary
693 networks. *Geochim. Cosmochim. Ac.* 72, 2695-2710, <https://doi.org/10.1016/j.gca.2008.03.018>.

694 Milnes, A.G., Corfu, F., 2011. Structural Geology and Tectonic Evolution of the Sognefjord
695 Transect, Caledonian Orogen, Southern Norway—A Field Trip Guide. *Geol. Soc. Am. Field Guide*
696 19 <https://doi.org/10.1130/2011.0019>.

697 Olsen, M.P., Scholz, C.H., Léger, A., 1998. Healing and sealing of a simulated fault gouge under
698 hydrothermal conditions: Implications for fault healing. *J. Geoph. Res.* 103, 7421-7430,

699 Pevear, D.R., 1999. Illite and hydrocarbon exploration. *P. Nat. Acad. Sci. USA* 96, 3440-3446,

700 Pleuger, J., Mancktelow, N., Zwingmann, H., Manser, M., 2012. K–Ar dating of synkinematic clay
701 gouges from Nealpine faults of the Central, Western and Eastern Alps. *Tectonophysics* 550-553,
702 1-16, <https://doi.org/10.1016/j.tecto.2012.05.001>.

703 Rutter, E.H., Holdsworth, R.E., Knipe, R.J., 2001. The nature and tectonic significance of fault-
704 zone weakening: an introduction. *Geol. Soc. London, Spec. Publ.* 186, 1-11,

705 Sasseville, C., Tremblay, A., Clauer, N., Liewig, N., 2008. K–Ar age constraints on the evolution of
706 polydeformed fold–thrust belts: The case of the Northern Appalachians (southern Quebec). *J.*
707 *Geodyn.* 45, 99-119, <https://doi.org/10.1016/j.jog.2007.07.004>.

708 Scheiber, T., Viola, G., 2018. Complex Bedrock Fracture Patterns: A Multipronged Approach to
709 Resolve Their Evolution in Space and Time. *Tectonics* 37, 1030-1062,
710 <https://doi.org/10.1002/2017tc004763>.

711 Scheiber, T., Viola, G., van der Lelij, R., Margreth, A., Schönenberger, J., 2019. Microstructurally-
712 constrained versus bulk fault gouge K-Ar dating. *J. Struct. Geol.* 127
713 <https://doi.org/10.1016/j.jsg.2019.103868>.

714 Surace, I.R., Clauer, N., Th  lin, P., Pfeifer, H.R., 2011. Structural analysis, clay mineralogy and K–
715 Ar dating of fault gouges from Centovalli Line (Central Alps) for reconstruction of their recent
716 activity. *Tectonophysics* 510, 80-93, <https://doi.org/10.1016/j.tecto.2011.06.019>.

717 Tagami, T., 2012. Thermochronological investigation of fault zones. *Tectonophysics* 538, 67-85,
718 <https://doi.org/10.1016/j.tecto.2012.01.032>.

719 Torgersen, E., Viola, G., Zwingmann, H., Harris, C., 2015a. Structural and temporal evolution of a
720 reactivated brittle-ductile fault - Part II: Timing of fault initiation and reactivation by K-Ar dating of
721 synkinematic illite/muscovite. *Earth Planet. Sc. Lett.* 410, 212-224,
722 <https://doi.org/10.1016/j.epsl.2014.11.013>.

723 Torgersen, E., Viola, G., Zwingmann, H., Henderson, I.H.C., 2015b. Inclined K-Ar illite age spectra
724 in brittle fault gouges: effects of fault reactivation and wall-rock contamination. *Terra Nova* 27, 106-
725 113, <https://doi.org/10.1111/ter.12136>.

726 van der Pluijm, B.A., Hall, C.M., Vrolijk, P.J., Pevear, D.R., Covey, M.C., 2001. The dating of
727 shallow faults in the Earth's crust. *Nature* 412, 172-174,

728 Verdel, C., van der Pluijm, B.A., Niemi, N., 2012. Variation of illite/muscovite 40 Ar/39 Ar age
729 spectra during progressive low-grade metamorphism: an example from the US Cordillera. *Contrib.*
730 *Mineral. Petr.* 164, 521-536, <https://doi.org/10.1007/s00410-012-0751-7>.

731 Viola, G., Scheiber, T., Fredin, O., Zwingmann, H., Margreth, A., Knies, J., 2016. Deconvoluting
732 complex structural histories archived in brittle fault zones. *Nat. Commun.* 7, 13448,
733 <https://doi.org/10.1038/ncomms13448>.

734 Viola, G., Torgersen, E., Mazzarini, F., Musumeci, G., van der Lelij, R., Sch  nenberger, J.,
735 Garofalo, P.S., 2018. New Constraints on the Evolution of the Inner Northern Apennines by K-Ar
736 Dating of Late Miocene-Early Pliocene Compression on the Island of Elba, Italy. *Tectonics*
737 <https://doi.org/10.1029/2018tc005182>.

738 Viola, G., Zwingmann, H., Mattila, J., Kapyaho, A., 2013. K-Ar illite age constraints on the
739 Proterozoic formation and reactivation history of a brittle fault in Fennoscandia. *Terra Nova* 25,
740 236-244, <https://doi.org/10.1111/ter.12031>.

741 Vrolijk, P., Pevear, D., Covey, M., LaRiviere, A., 2018. Fault gouge dating: history and evolution.
742 *Clay Minerals* 53, 305-324, <https://doi.org/10.1180/clm.2018.22>.

743 Walsh, E.O., Hacker, B.R., Gans, P.B., Wong, M.S., Andersen, T.B., 2013. Crustal exhumation of
744 the Western Gneiss Region UHP terrane, Norway: 40Ar/39Ar thermochronology and fault-slip
745 analysis. *Tectonophysics* 608, 1159-1179, <https://doi.org/10.1016/j.tecto.2013.06.030>.

- 746 Weisenberger, T., Bucher, K., 2010. Zeolites in fissures of granites and gneisses of the Central
747 Alps. *J. Metamorph. Geol.* 28, 825-847, <https://doi.org/10.1111/j.1525-1314.2010.00895.x>.
- 748 Whitney, D.L., Evans, B.W., 2010. Abbreviations for names of rock-forming minerals. *Am. Miner.*
749 95, 185-187, <https://doi.org/10.2138/am.2010.3371>.
- 750 Yamasaki, S., Zwingmann, H., Yamada, K., Tagami, T., Umeda, K., 2013. Constraining the timing
751 of brittle deformation and faulting in the Toki granite, central Japan. *Chem. Geol.* 351, 168-174,
752 <https://doi.org/10.1016/j.chemgeo.2013.05.005>.
- 753 Zwingmann, H., Mancktelow, N., 2004. Timing of Alpine fault gouges. *Earth Planet. Sc. Lett.* 223,
754 415-425, <https://doi.org/10.1016/j.epsl.2004.04.041>.

755

756 **Appendix**

757 The mineralogical composition of all grain size fractions was studied with X-ray diffraction
758 (XRD). Randomly-oriented samples were prepared by side-loading and analysed with a
759 Bruker D8 Advance X-ray diffractometer operating with a Cu X-ray tube (40 kV/40 mA) and
760 Lynxeye XE detector. XRD scanning was performed from 3 to 75° 2 θ with a step size of
761 0.02° 2 θ , a measurement time of 1 s per step, and rotation speed of 30° per minute. Fixed
762 divergence had an opening of 0.6 mm and primary and secondary soller slits were 2.5°. A
763 knife edge was used to reduce scatter radiation. Mineral identification was carried out with
764 the automatic and/or manual peak search-match function of Bruker's Diffrac.EVA V4.2
765 software using both Crystallographic Open Database (COD) as well as the PDF 4 Minerals
766 database from the International Centre for Diffraction Data (ICDD). For further clay
767 minerals study, oriented mounts of fractions 2-6 μ m were prepared by letting 1 ml of
768 sample suspension dry out on a glass slide. These slides were measured from 2 to 40° 2 θ
769 at room temperature, after treatment with ethylene glycol for 24 h, and after heating at 550
770 °C for 1 h

771 The procedure followed to perform K-Ar dating of each grain size fractions starts with
772 packing aliquots of air-dry clay samples in molybdenum foil. They are weighed using a
773 Mettler Toledo XPE26DR microbalance, with a resolution of 2 μ g and a combined
774 weighing uncertainty of 4 μ g. Samples are degassed at 1400 °C for 10 minutes. The

775 evolved gas is spiked with a known amount of isotopically pure ^{38}Ar and purified in two
776 stages with a Titanium Sublimation Pump and a combination of two SAES GP50 ST101
777 getters, one at 300 °C and one at 22 °C. The purified argon is analysed in static vacuum in
778 an IsotopX NGX multicollector noble gas mass spectrometer using faraday cups with
779 1012 Ω amplifiers for ^{38}Ar and ^{36}Ar and a 1111 Ω amplifier for ^{40}Ar ; the gas is analysed for
780 600 integrations of 1 second. Baseline corrected volts are regressed back to inlet time
781 using an exponential best fit regression function. Blanks are run periodically. Mass bias
782 corrections are performed using a power law on blank corrected intercept values by using
783 within-batch air analyses compared with the atmospheric $^{40}\text{Ar}/^{36}\text{Ar}$ composition of $298.56 \pm$
784 0.31 (Lee et al., 2006). The ^{38}Ar spike is calibrated using HD-B1 biotite (Fuhrmann et al.,
785 1987) with a $^{40}\text{Ar}^*$ concentration of $3.351 \times 10^{-11} \text{ mol/g}$ (Charbit et al., 1998). Long term
786 reproducibility of many aliquots of HD-B1 biotite is better than 0.3% RSD.

787 Potassium concentrations are determined by fluxing approximately 50 mg of clay sample
788 in lithium tetraborate. The resulting glass is dissolved in HNO_3 spiked with a known
789 concentration of Rh as internal standard. The K concentration is analysed using a Perkin
790 Elmer Optima 4300DV ICP-OES. The uncertainty of K determination is estimated from
791 evaluating the accuracy of several whole rock standards with similar K concentration range
792 and is better than 2%.

793 Radiogenic $^{40}\text{Ar}^*$ concentrations, relative uncertainties, and K-Ar ages are calculated
794 using the equation of Hałas and Wójtowicz (2014), using the decay constants of Renne et
795 al. (2011).

796 Charbit, S., Guillou, H. and Turpin, L., 1998. Cross calibration of K–Ar standard minerals using an
797 unspiked Ar measurement technique. *Chem. Geol.* 150(1-2), 147-159.

798 Fuhrmann, U., Lippolt, H. and Hess, J.C., 1987. HD-B1 biotite reference material for K-Ar
799 chronometry. *Chem. Geol.* 66, 41-51.

800 Hałas, S., Wójtowicz, A., 2014. Propagation of error formulas for K/Ar dating method.
801 *Geochronometria* 41, 202-206. <https://doi.org/10.2478/s13386-013-0162-1>

802 Lee, J.Y., Marti, K., Severinghaus, J.P., Kawamura, K., Yoo, H.S., Lee, J.B. and Kim, J.S., 2006. A
803 redetermination of the isotopic abundances of atmospheric Ar. *Geochim. Cosmochim. Ac.* 70,
804 4507-4512. <https://doi.org/10.1016/j.gca.2006.06.1563>

805 Renne, P.R., Balco, G., Ludwig, K.R., Mundil, R., Min, K., 2011. Response to the comment by
806 W.H. Schwarz et al. on "Joint determination of ^{40}K decay constants and $^{40}\text{Ar}^*/^{40}\text{K}$ for the Fish
807 Canyon sanidine standard, and improved accuracy for $^{40}\text{Ar}/^{39}\text{Ar}$ geochronology" by P.R. Renne et
808 al. (2010). *Geochim. Cosmochim. Ac.* 75, 5097-5100. <https://doi.org/10.1016/j.gca.2011.06.021>

Figure1

[Click here to download Figure: Figure1.pdf](#)

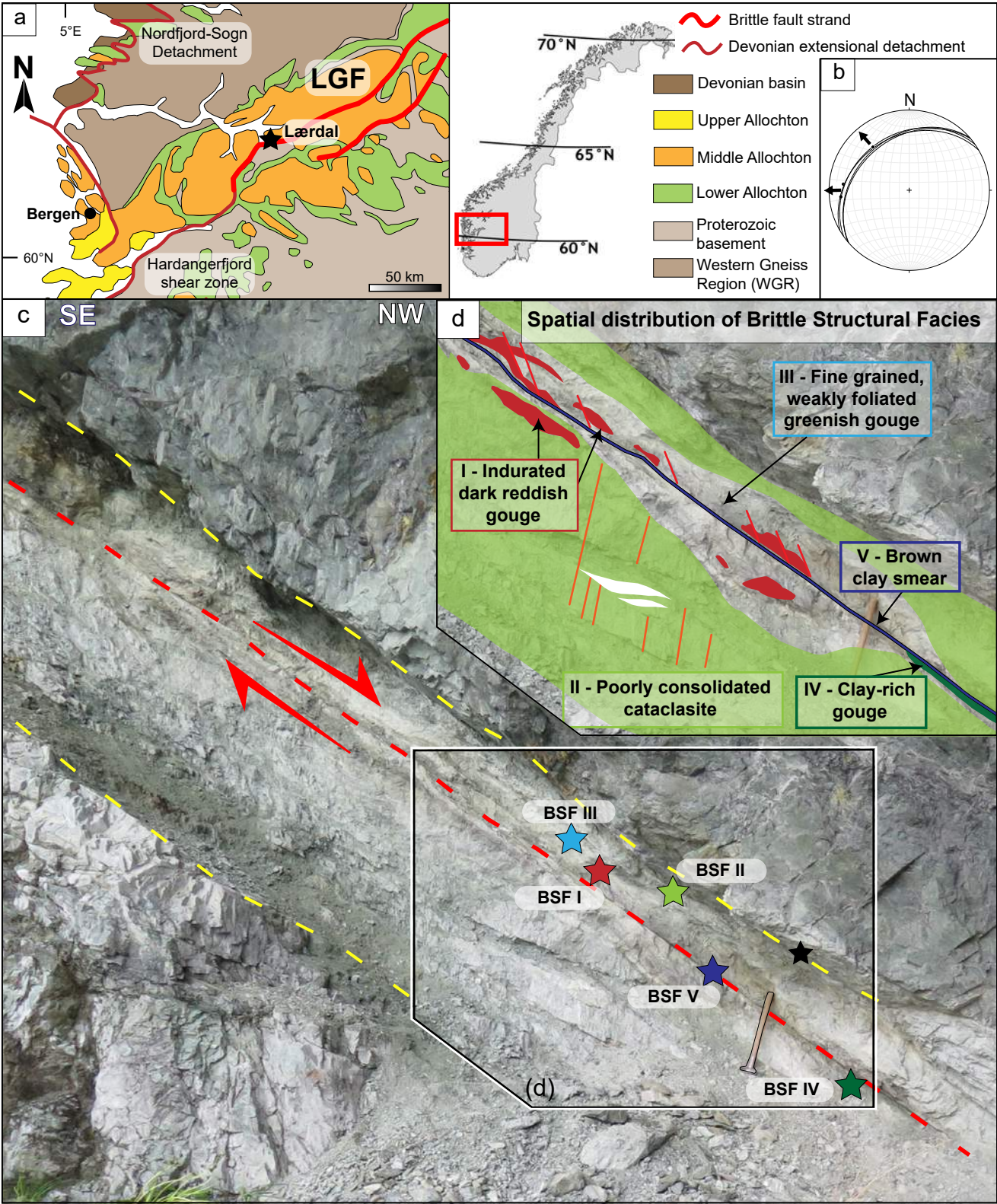


Figure2

[Click here to download Figure: Figure2.pdf](#)

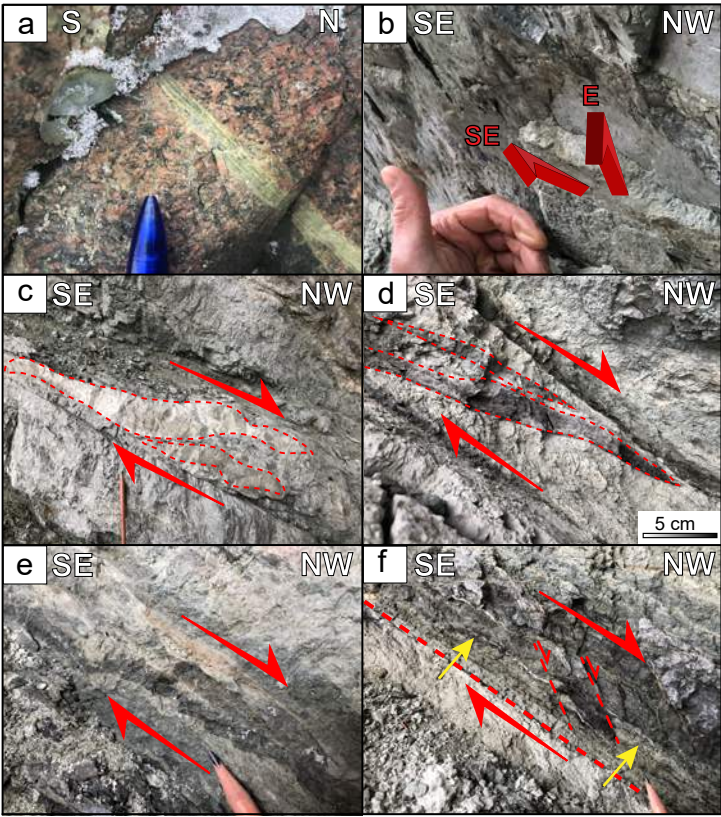


Figure3
[Click here to download Figure: Figure3.pdf](#)

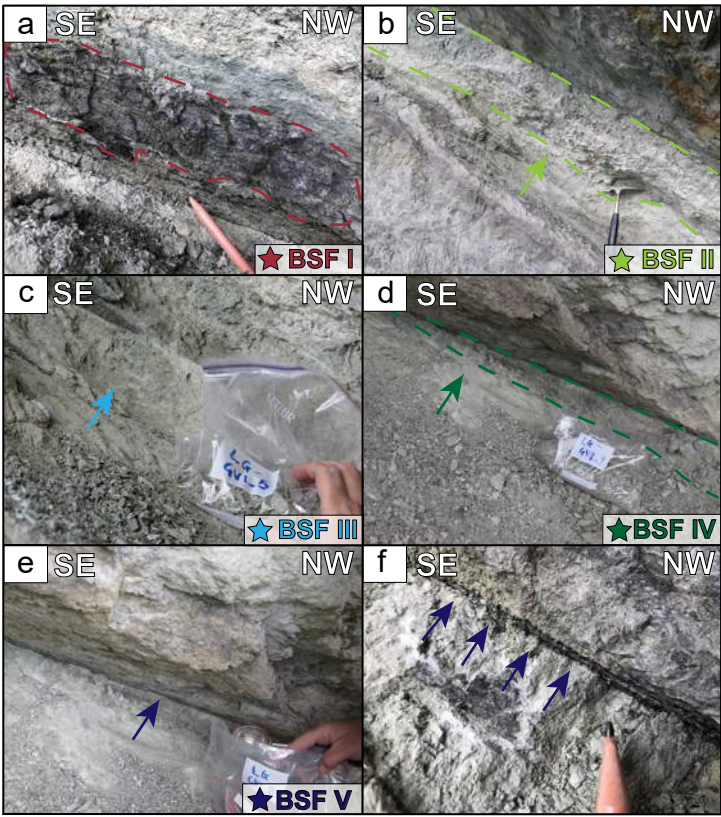


Figure4

[Click here to download Figure: Figure4.pdf](#)

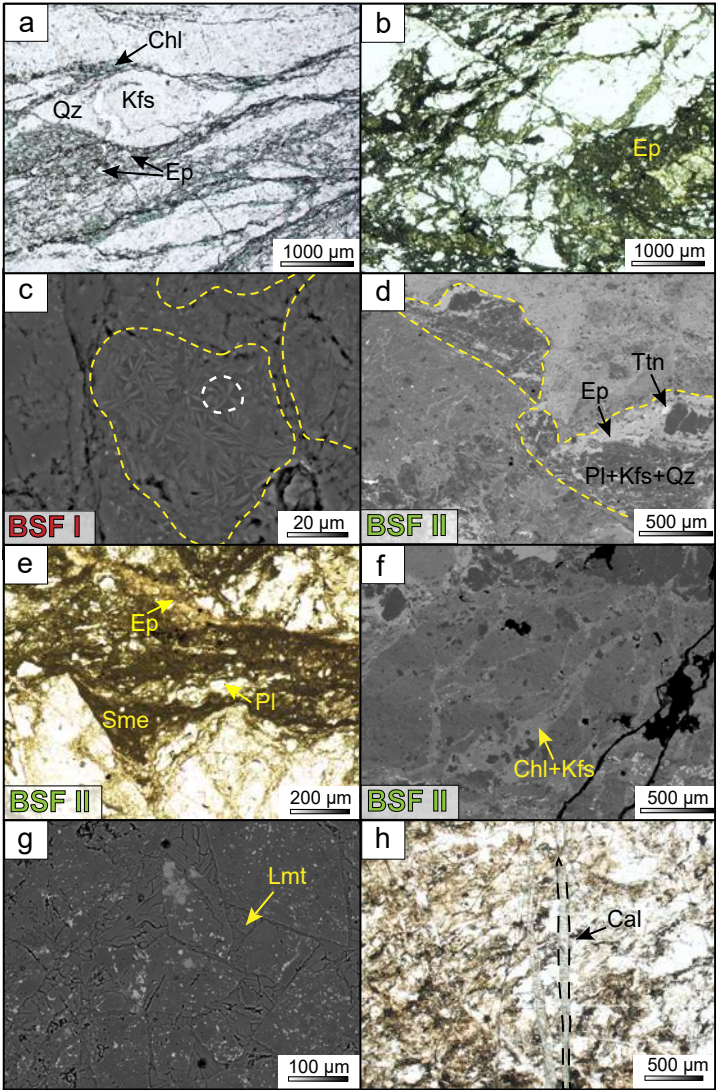


Figure5
Click here to download Figure: Figure5.pdf

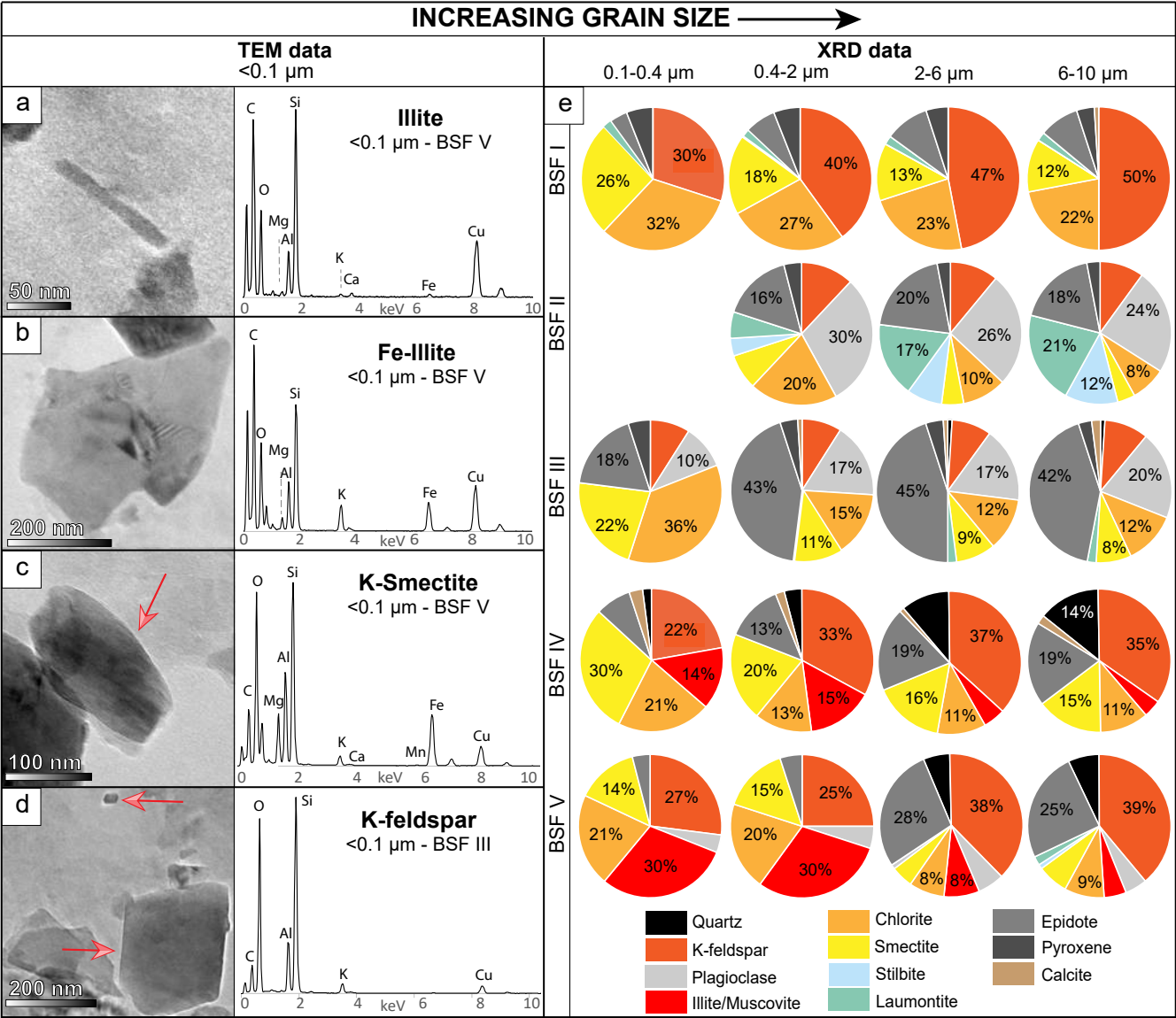


Figure6

[Click here to download Figure: Figure6.pdf](#)

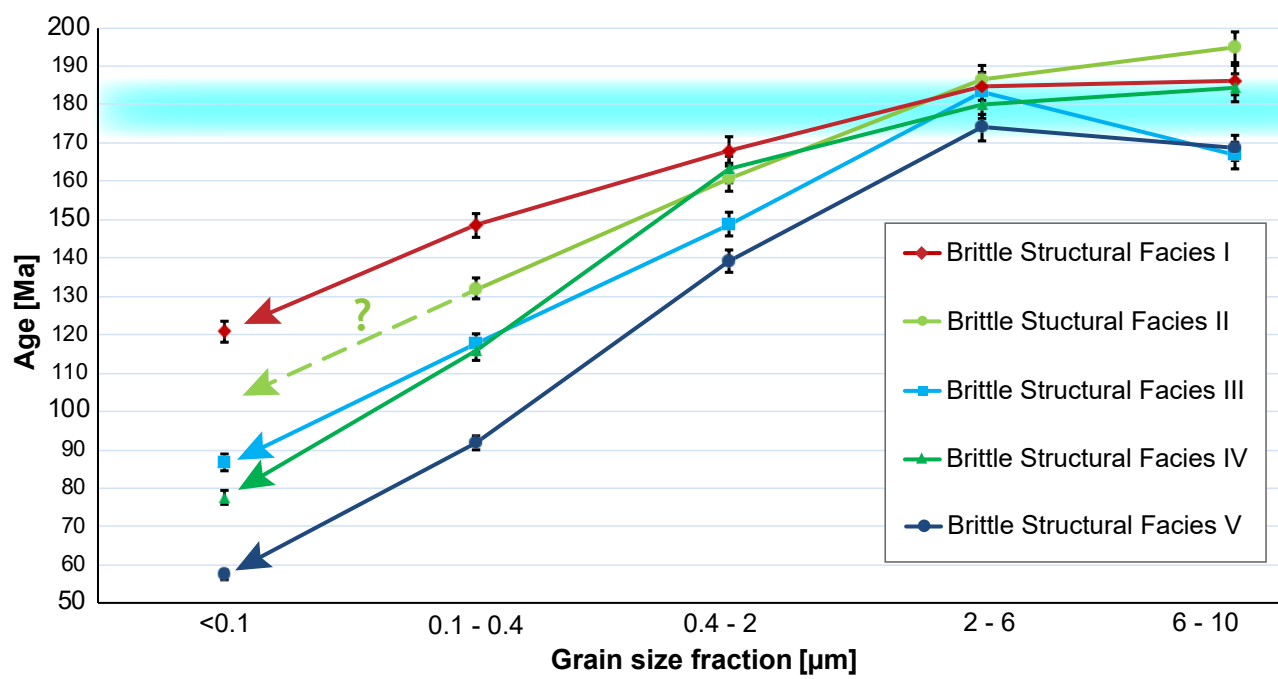


Figure7
Click here to download Figure: Figure7.pdf

